Modelling methane-air turbulent diffusion flame in a gas turbine combustor with artifical neural network

N. S. Mehdizadeh **P. Sinaei**
sinaei@aut.ac.ir
Centre of Excellence in Computational Aerospace Engineering
Aerospace Engineering Department
Amirkabir University of Technology
Tehran, Iran

ABSTRACT

The present paper reports a way of using an artificial neural network (ANN) for modelling methane-air jet diffusion turbulent flame characteristics, such as temperature and chemical species mass fractions in a gas turbine combustion chamber. Since the neural network needs sets of examples to adapt its synaptic weights in the training phase, we used pre-assumed probability density function (PDF) method and considered chemical equilibrium chemistry model to compute the flame characteristics for generating the examples of input-output data sets. In this approach, flow and mixing field results are presented with a non-linear first order k-ε model. The turbulence model is applied in combination with pre-assumed β-PDF modelling for turbulence-chemistry interaction. The training algorithm for the neural network is based on a back-propagation supervised learning procedure, and the feed-forward multi-layer network is incorporated as neural network architecture. The ability of ANN model to represent a highly non-linear system, such as a turbulent non-premixed flame is illustrated, and it can be summarized that the results of modelling of the combustion characteristics using ANN model are satisfactory, and the CPU-time and memory savings encouraging.

NOMENCLATURE

E error function (–)
f mixture fraction (–)
g mixture fraction variance (–)
k turbulent kinetic energy (m^2/s^2)
P_k production rate of kinetic energy (m^2/s^3)
S_{ij} ij-component of strain rate tensor (1/s)
t time (s)
T temperature (K)
v_i i-component of velocity vector (ms^{-1})
x_i Eulerian i-co-ordinate (m)
w synaptic weight (–)
y expected output (–)
$\hat{y}$ estimated output (–)
Y species mass fraction (–)
α neural network momentum factor (–)
χ scalar dissipation rate (1/s)
δ Kronecker delta (–)
ε turbulent dissipation rate (m^2/s^3)
η neural network learning rate (–)
μ viscosity (Pa.s)
θ bias value (–)
ρ density (kg/m^3)
τ_t turbulent time scale (s)

1.0 INTRODUCTION

Highly non-linear nature of chemical reactions in high temperatures and the fluctuations in density, pressure, velocity and concentration of chemical species are the main outstanding problems in turbulent combustion. Governing differential equations have complicated forms in turbulent reacting flows and they need lengthy, complicated and time consuming computer codes and high CPU-time and RAM storage requirements to be solved. Therefore, we need some particular methods to calculate the mean flow field and thermo-chemical state. Direct numerical simulation (DNS)[1] and probability density function (PDF)[2] are examples of these methods for turbulent combustion modelling.

Paper No. 3289. Manuscript received 17 March 2008, revised version received 4 November 2008, accepted 30 June 2009.

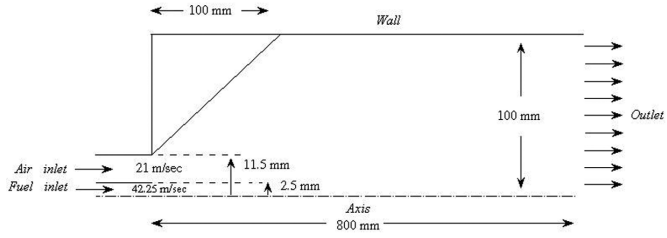

Figure 1. Schematic diagram of combustion chamber.

Recently, several techniques to handle chemical models have been proposed. Examples of such procedures are the *in-situ* Adaptive tabulation (ISAT)[3] and the intrinsic low dimension manifold (ILDM)[4]. These techniques are based on the storage of a large number of species increments for different points in the chemical-composition space. It is obvious that the main disadvantage of these techniques is the fast growth of memory requirements as the number of chemical species increases.

Artificial neural network (ANN) modelling is a rapidly expanding field of research and application. A neural network is a massively parallel dynamic structure and the neural modelling is to train the computing system for capturing the principles of a physical problem and generating a model. This model produces an approximation of the real system while retaining the same general behaviour.

Artificial neural networks emerge as a general, fast and compact way of modelling complex dynamical systems, of which a turbulent combustion is a good example. The main feature of ANNs are their ability to model complex, non-linear problems by being presented with examples, or sets of input-output patterns.

An ANN consists of interconnected layers of non-linear processing elements. The network saves the information using its synaptic weights. These weights are adjusted during an iterative process called a learning phase in which all the examples are presented to ANN repeatedly. After the learning phase, ANN can be used to find the answer to an input pattern. Using this technique, good results can be achieved with a low processing time and small memory requirements.

In this paper a turbulent methane-air diffusion flame in a gas turbine combustor has been modelled with an artificial neural network. The examples or input-output patterns for the training phase have been generated from pre-assumed PDF solution using chemical equilibrium chemistry model. In this part of the paper, the relative importance of the turbulence model choice and the chemistry model is discussed in the framework of pre-assumed β-PDF modelling for turbulence-chemistry interaction, with mixture fraction as a conserved scalar. The important turbulence model feature is the transport equation for the dissipation rate by following the idea of Shih *et al*[5]. This transport equation is based on a modelled transport equation for mean enstrophy (square of the vorticity fluctuations). In the training phase, backpropagation learning algorithm is used. Radial distribution of themorchemical parameters in various sections of combustion chamber are calculated with ANN and compared with the PDF solution.

2.0 THE COMBUSTION CHAMBER

The schematic diagram of the combustion chamber is shown in Fig. 1. This combustion chamber has been modelled by Yaga and Sasada[6] with large eddy simulation (LES) method. In Ref. 6, Yaga and Sasada constructed an eddy characteristic time derived from large-scale motion to calculate the combustion reaction rate. They also used a three step global reaction mechanism for the methane-air combustion. The coaxial combustor has 200mm, in internal diameter, and 800mm, in length. The inner pipe diameter is 5mm and the annulus pipe diameter is 23mm.

Table 1
Velocity and temperature of inlet fuel and oxidiser

	V(ms^{-1})	T(K)
Methane	21	293·15
Air	42·25	293·15

Table 2
Overview of turbulence model parameters

Parameter	$c_{\varepsilon 1}$	$c_{\varepsilon 2}$	C_1	σ_ε	σ_k
Value	1.44	$\max\{1.9 f_\beta, 1.83+\frac{0.075\Omega\tau_t}{1+S^2\tau_t^2}\}$	$\max\{0.43, \frac{S\tau_t}{5+S\tau_t}\}$	1.00	1.20

Table 1 shows the temperature and velocity of inlet fuel and oxidiser. The equivalence ratio is considered as $\phi = 1{\cdot}00$.

3.0 MODEL DESCRIPTION

3.1 Turbulence model

A non-linear first order expression for the turbulent stresses in terms of the local mean strain rate and vorticity tensors is applied, which is good enough to obtain accurate results for a wide variety of flow types[7]:

$$-\bar{\rho}\overline{u_i'' u_j''} = 2\mu_t S_{ij} - \frac{2}{3}\rho k \delta_{ij} \quad \ldots (1)$$

And the transport equations for the turbulence quantities are:

$$\begin{cases} \dfrac{\partial}{\partial x_m}(\rho k u_m) = P_k - \rho\varepsilon + \dfrac{\partial}{\partial x_m}[(\mu + \dfrac{\mu_t}{\sigma_k})\dfrac{\partial k}{\partial x_m}] \\ \dfrac{\partial}{\partial x_m}(\rho\varepsilon u_m) = (1-f_\beta)c_{\varepsilon 1}\dfrac{P_k}{\tau_1} + f_\beta C_1 S\rho\varepsilon \\ -c_{\varepsilon 2} f_2 \rho\dfrac{\varepsilon}{\tau_t} + \dfrac{\partial}{\partial x_m}[(\mu + \dfrac{\mu_t}{\sigma_\varepsilon})\dfrac{\partial \varepsilon}{\partial x_m}] + E \end{cases} \quad \ldots (2)$$

The source term in the ε transport equation is a blending of the turbulent kinetic energy divided by the turbulence time scale in the neighbourhood of the solid boundaries and a source term derived from a modelled enstrophy transport equation[5]. The boundary conditions at a solid boundary are $k = 0$ and $\varepsilon = 2(\mu/\rho)(\partial\sqrt{k}/\partial n)^2$ Table 2 shows the parameters of turbulence model.

3.2 Chemistry model

The chemical reaction model is one the most important parameters in modelling a turbulent nonpremixed combustion[8]. For the pre-assumed PDF simulations, the chemical model is full chemical equilibrium. The main species are (maximum mean mass fraction in the field larger than 10^{-7}) CH_4, O_2, CO_2, CO, H_2O, OH, H_2, O, HO_2, H, NO, NO_2, N_2 and C_2H_6.

3.3 Turbulence-chemistry interaction model

The non-premixed modelling approach involves the solution of transport equations for one or two conserved scalars (the mixture fractions). Equations for individual species are not solved. Instead, species concentrations are derived from the predicted mixture fraction fields.

The basis of the non-premixed modelling approach is that, under a certain set of simplifying assumptions, the instantaneous thermo-

https://doi.org/10.1017/S0001924000003195 Published online by Cambridge University Press

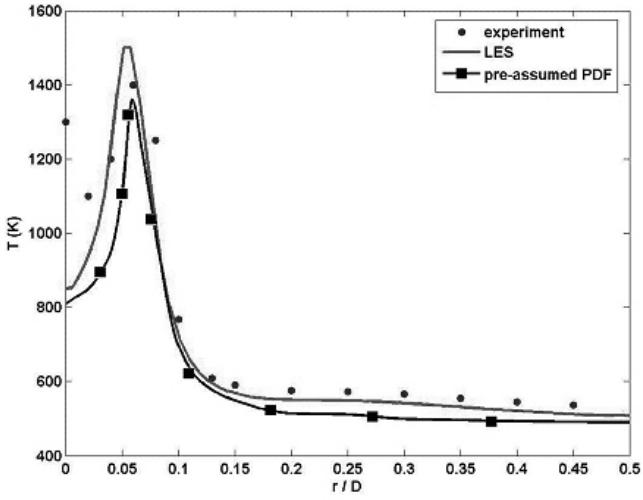

Figure 2. Radical distribution of temperature at x = 100mm.

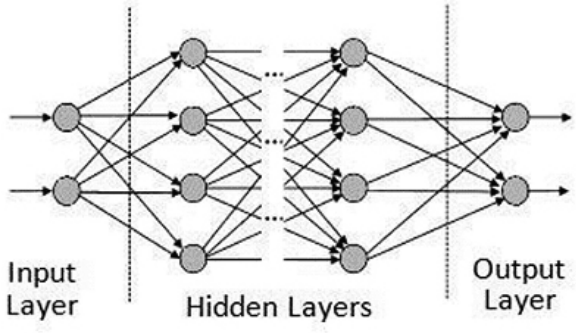

Figure 3. Schematic diagram of a feed-forward multilayer neural network.

chemical state of the fluid is related to a conserved scalar quantity, known as the mixture fraction, f. The mixture fraction is the normalised mass fraction of an atomic element originating from one of the input streams, usually, the fuel stream[9].

Under the assumption of equal diffusivities, the species equations can be reduced to a single equation for the mixture fraction, f. The reaction source terms in the species equations cancel, and thus, f is a conserved quantity. While the assumption of equal diffusivities is problematic for laminar flows, it is generally acceptable for turbulent flows, where turbulent convection overwhelms molecular diffusion.

The steady-state transport equations for the mean mixture fraction, $\bar{f}$, and its variance, $\bar{g} = \overline{f'^2}$, are standard:

$$\frac{\partial}{\partial x_m}(\rho \bar{f} u_m) = \frac{\partial}{\partial x_m}[\frac{\mu_t}{\sigma_\varepsilon}\frac{\partial \bar{f}}{\partial x_m}] \quad \ldots (3)$$

$$\frac{\partial}{\partial x_m}(\rho \bar{g} u_m) = \frac{\partial}{\partial x_m}[\frac{\mu_t}{\sigma_g}\frac{\partial \bar{g}}{\partial x_m}] + 2\frac{\mu_t}{\sigma_\varepsilon}\frac{\partial \bar{f}}{\partial x_m}\frac{\partial \bar{f}}{\partial x_m} - \rho\chi \quad \ldots (4)$$

Since the molecular diffusion is neglected in Equations (4) and (5), only the turbulent diffusion, modelled by the linear gradient diffusion hypothesis, is accounted for. For the pre-assumed PDF, β-PDFs are used. The turbulent Schimdt numbers are $\sigma_g = \sigma_\varepsilon = 0{\cdot}85$, which is higher than the standard value of 0·7. In Ref. 10 it was explained that near the axis, the eddy viscosity is higher with the present model than what is obtained with the k-ε model. As a consequence, the mixture fraction spreading rate is over-estimated with the standard value of $\sigma_g = \sigma_\varepsilon = 0{\cdot}7$.

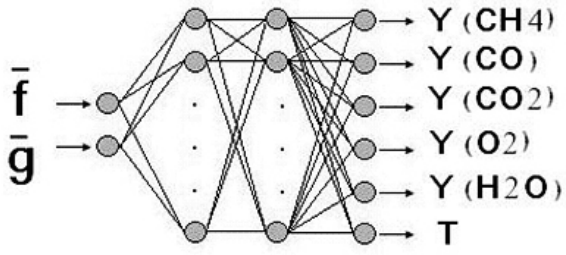

Figure 4. Schematic diagram of used neural network.

Finally the mean scalar dissipation rate is modelled as:

$$\chi = 2g(\varepsilon / k) \quad \ldots (5)$$

Figure 2 shows the radial distribution of temperature at an arbitrary section of the combustor, x = 100mm. LES and experiment results are reported in Ref. 6. Good agreements are seen in our solution (pre-assumed PDF) and LES method which is reported in Ref. 6. For the centerline, the reason why thermocouple system indicates exceed temperature is that the effect of radiation from suction pyrometer tip is large. Accordingly, applied PDF solution seems to be convenient for training the neural network.

4.0 FEED-FORWARD NEURAL NETWORK ARCHITECTURE

As shown in Fig. 3, a feed-forward multilayer neural network is a computing architecture that consists of massively distributed interconnected simple neurons. For multilayer perceptron networks, the inputs propagate through the network, and the output of each neuron is evaluated according to:

$$y^n{}_i = f(\sum_{j=1}^{K_{n-1}} w_{ij}{}^n y_j{}^{n-1} + \theta_i{}^n)_{i=1,\ldots,K_n \& n=1,\ldots,N} \quad \ldots (6)$$

where y_i^n is the output of the ith neuron of the nth layer, w_{ij}^n is the synaptic weight value of connection between jth node of the (n–1)th layer and ith neuron of nth layer, and, finally, θ_i^n is the bias value of the ith neuron of the nth layer. The nonlinear activation function, f(.), is differentiable, and it must have a positive first derivative.

In this work multilayer perceptron architecture, with two intermediate or hidden layers, has been employed. Each hidden layer consists of 20 neurons. A hyperbolic-tangent function has been used as the transfer function. Figure 4 shows the neural network, we used for modelling the combustor. The inputs of the network are mean mixture fraction, $\bar{f}$, and mean mixture fraction variance, $\bar{g} = \overline{f'^2}$. The output consists of six scalars, mass fractions of CH_4, O_2, H_2O and CO_2 and temperature.

5.0 THE LEARNING ALGORITHM

5.1 The back-propagation algorithm

Figure 5 shows the synaptic weights between the neurons in different layers[12]. For adjusting the weights, w_{ij}^n, in the network, we used the back-propagation method. This method is probably the most well known and widely used learning algorithm that is based on gradient descent technique[11]. This algorithm minimises the value

https://doi.org/10.1017/S0001924000003195 Published online by Cambridge University Press

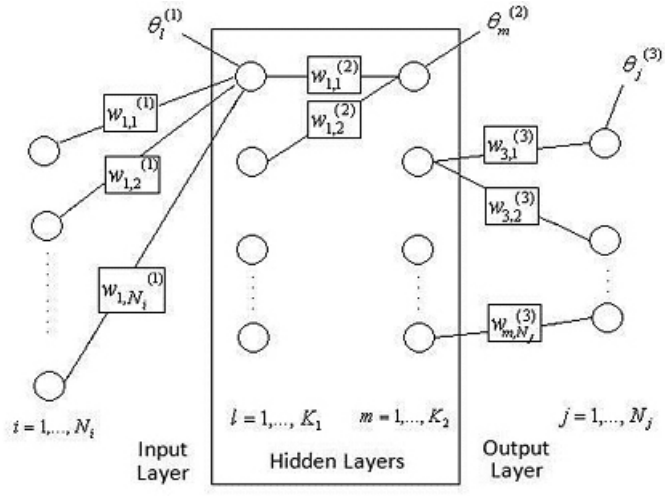

Figure 5. Synaptic weights for the neural network with two hidden layers.

of the error function during the learning process. The error function, E, is defined as:

$$E = \sum_{k=1}^{m} \sum_{i=1}^{n_o} (y_{i,k} - \hat{y}_{i,k})^2 \quad \ldots (7)$$

where n_o is the number of output units, y_k and $\hat{y}_k$ are the expected and estimated outputs for the kth learning pattern.

The back-propagation method adjusts the weights according to the following equation:

$$w_{ij}{}^n(t+1) = w_{ij}{}^n(t) + \eta \delta_j \hat{y}_i + \alpha[w_{ij}{}^n(t) - w_{ij}{}^n(t-1)] \quad \ldots (8)$$

where t is the iteration number, and, η and α are learning and momentum factors, respectively. These factors can be adjusted to speed up the convergence of the algorithm. Furthermore, the use of appropriate η and α reduces the possibility of being trapped in a local minimum. The function represents the change in the error function of the jth node with respect to the network inputs. It is:

$$\delta_j = -\frac{\partial E_t}{\partial \sum w_{ij}{}^n \hat{y}_i} \quad \ldots (9)$$

The explicit form of δ_j depends on the activation function. It should be mentioned that j is an internal or an output node. The functional form of δ_j is given by:

$$\delta_j = \begin{cases} f'_j(y_j - \hat{y}_j) & j: output \quad node \\ f'_j \sum_i \delta_i w_{ij}{}^n & j: internal \quad node \end{cases} \quad \ldots (10)$$

The function f'_j denotes the derivative of the activation function of the jth node with respect to the total net inputs. It is:

$$f'_j = \frac{\partial \hat{y}_i}{\partial \sum_i w_{ij} \hat{y}_i} \quad \ldots (11)$$

5.2 Example generation for the learning patterns

Appropriate distribution of the learning patterns increases the accuracy of the network[13]. On the other hand, the input-out pairs of the training phase must be properly distributed to cover the whole compositional space. This domain is [0, 1] for the mixture fraction and $[0, \sqrt{\bar{f}(1-\bar{f})}]$ for the mixture fraction variance, as the inputs of the network. The allowable domain of mixture fraction has been divided into small intervals of 0·005. Since, around the stoichiometric point (f_{st} = 0·0552), the effects of nonlinearities are larger, the step for the intervals is decreased to 0·0002 in this zone. The allowable domain of mixture fraction variance is divided into 12 equal intervals. With such a partitioning of the allowable space, we have 2,976 patterns for the training phase.

Table 3
Training-set error (first figure) and test-set error (second figure) as a function of the number of hidden units

Hidden units	1×10	1×16	2×10	2×20
Error (training-set/test-set)	0·164/0·354	0·125/0·324	0.011/0.102	0·003/0·0854

5.3 Scaling

After selecting the training data set, some pre-processing must be applied to the input and out values, before they can be fed into the neural network for the training[14]. Using Equations 14 and 15, a transformation is applied to map the data in the optimal working range. The ANN theory shows that this optimal range for inputs and outputs is [–1, +1]. First the data are transformed to achieve zero mean and unity variance:

$$x'_j = \frac{x_j - \bar{x}_j}{\sigma_{x_j}} \quad \ldots (12)$$

where x'_j is the value of jth input or jth output, and $\bar{x}_j$ and σ_{xj} are the average and standard deviation of all the values, respectively. After this transformation, a range adjustment transformation is used to map the data in the optimal range:

$$x''_j = 2\frac{x'_j - \min\{x'_j\}}{\max\{x'_j\} - \min\{x'_j\}} - 1 \quad \ldots (13)$$

where x^n_j is the x'_j value adjusted to the optimal range [–1 , +1].

5.4 ANN architecture optimisation

The topology of the feed-forward ANN can be described in terms of the number of intermediate (hidden) layers of neurons and the number of neurons in each layer. The ANN architecture is to be chosen in a trial and error process to maximise the quality of the fitting of the data set. If the number of adjustable parameters in an ANN is too large, then the ANN provides accurate answers for the data which has been used in the training phase, but it yields poor answers for unseen data. This problem is called overfitting. To avoid overfitting, the performance of the ANN is measured during the learning process using another set of examples called the test set. Accordingly, several ANN architectures have been trained for the present case, and the performance of each of them has been measured.

The errors of the training set and the test set patterns are shown in Table 3. These errors are calculated by applying Equation (9) separately to the training set and the test set patterns. Table 3 shows that the error in all cases decreases as the number of hidden units is increased. Trials have been performed also for 2 × 25 and 2 × 30 neurons but the improvements in errors were very small. Therefore, the 2 × 20 architecture is picked as the optimised ANN architecture. Table 3 also shows that in all cases the test set error is higher than the training error. This is the usual and intrinsic behavior of any ANN.

https://doi.org/10.1017/S0001924000003195 Published online by Cambridge University Press

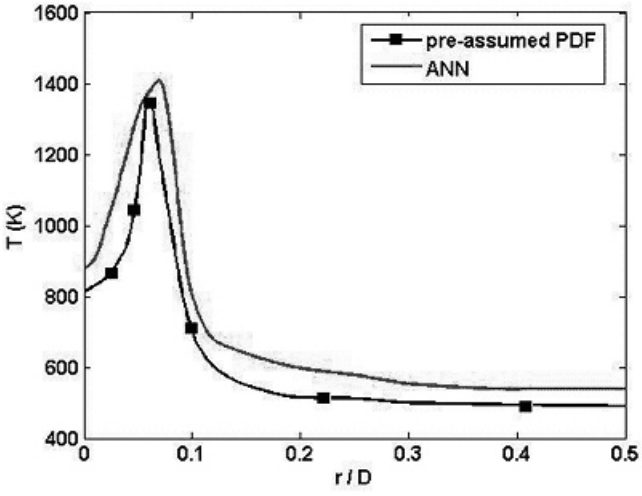

Figure 6. Radial distribution of temperature at x = 100mm.

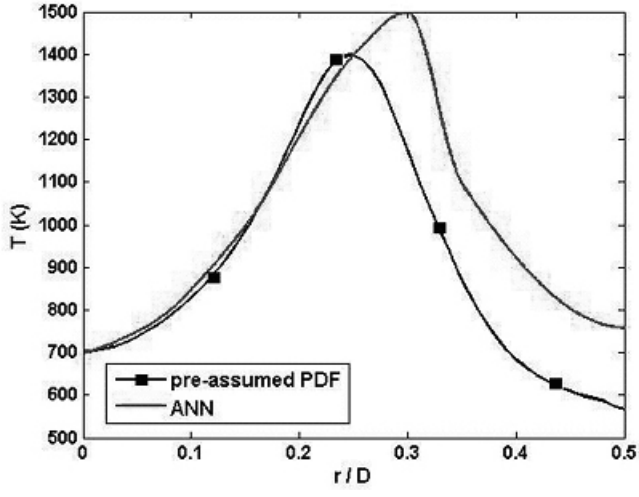

Figure 7. Radial distribution of temperature at x = 400mm.

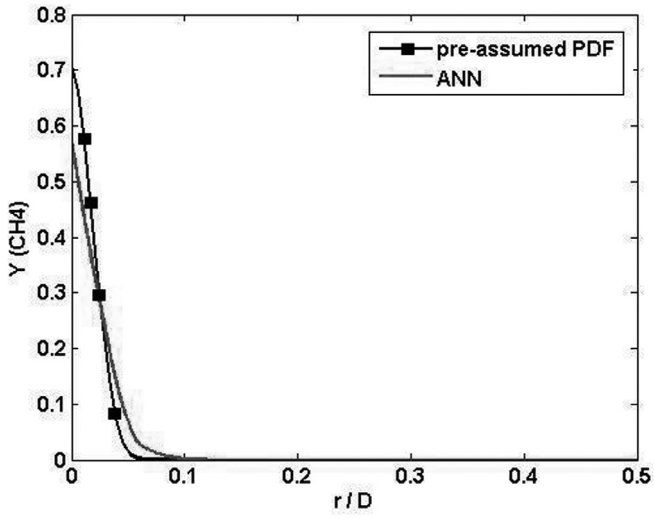

Figure 8. Radial distribution of methane mass fraction at x = 100mm.

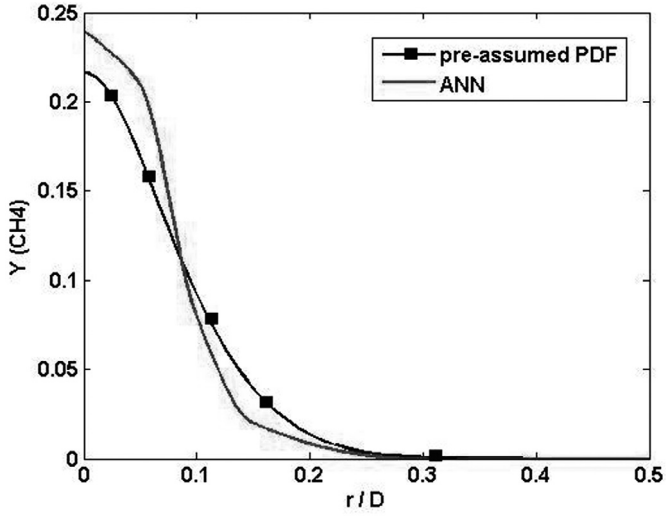

Figure 9. Radial distribution of methane mass fraction at x = 400mm.

6.0 RESULTS

The results of neural modelling of the methane-air turbulent combustion system are presented in this section. The following figures correspond to the radial distribution of temperature and mass fraction of species in two different sections of the combustion chamber: at x = 100mm and x = 400mm.

Figure 6 shows the radial distribution of the temperature at section x = 100mm which is computed by pre-assumed PDF solution and modelled by the neural network. In Fig. 7 we can see the same distribution at another section of the combustion chamber at x = 400mm. Radial distribution for the methane mass fraction in these two sections is shown in Figs 8 and 9. Based on these four figures, it can be concluded that there is, fairly, a good agreement between PDF solution and neural modelling. Figures 10 and 11 show the distribution of mass fraction for the oxygen and an intermediate species, carbon monoxide and finally Fig. 12 shows the radial distribution of mass fraction for another important product of combustion, H_2O at section x = 100mm.

All the figures show that, in the regions which are far from the rich region of the flame, the accuracy of neural network model is good and there is considerable coincidence between presumed PDF approach and neural model in this region. In rich region of the flame, there are some inconsistency between the prediction of neural network and presumed PDF model. The reason refers to highly non-linear treatment of the combustion process in this region. The outputs of the neural network become highly non-linear functions of the inputs due to the variations and non-linear treatment of the chemical reaction rates around the stoichiometric point of combustion.

For this study, the numerical computations have been performed on a computer with Intel Core2 Duo CPU, 2·4 GHz and 2·00 GB memory. A brief comparative study of computational cost with respect to time shows that the neural network modelling is up to ten times faster than the presumed PDF modelling.

7.0 CONCLUSIONS AND FUTURE WORKS

This paper has illustrated how a neural network can be advantageously used to model various thermo chemical quantities of a turbulent diffusion flame in various sections of the combustion chamber, with considerable time saving (when compared with LES and presumed PDF methods). Also the approach for building the neural network and using the adequate training samples has been stressed.

https://doi.org/10.1017/S0001924000003195 Published online by Cambridge University Press

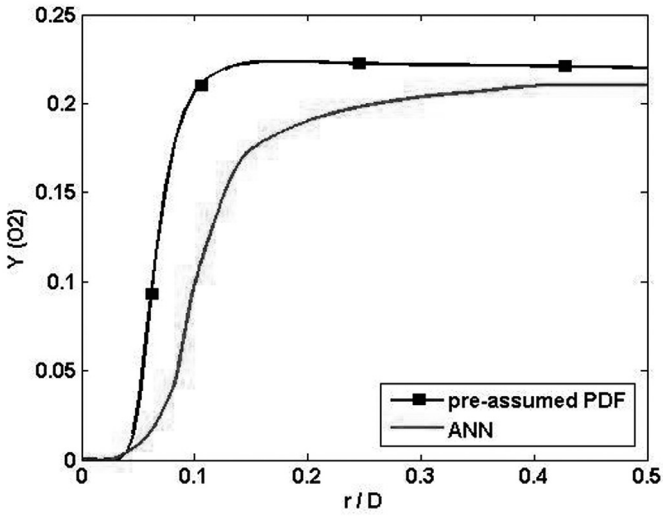

Figure 10. Radial distribution of oxygen mass fraction at x = 100mm.

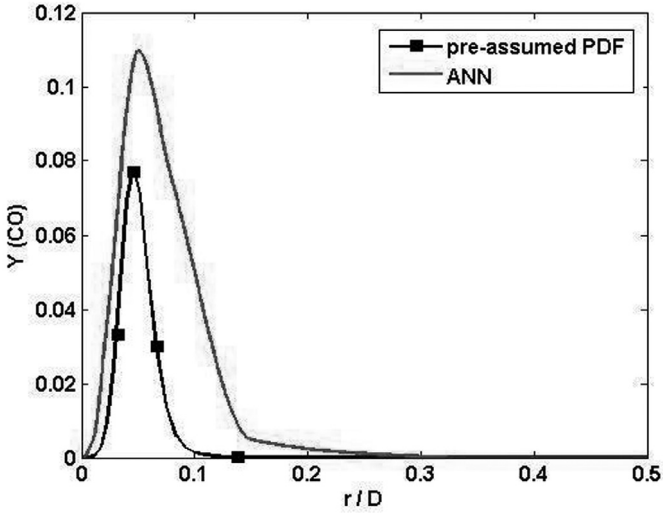

Figure 11. Radial distribution of CO mass fraction at x = 100mm.

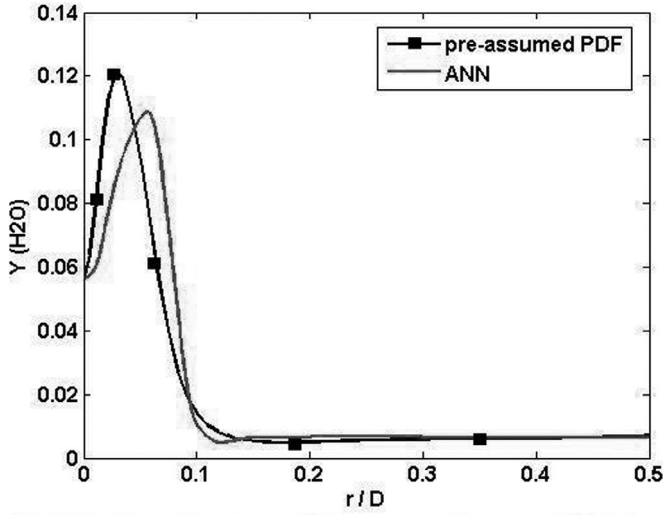

Figure 12. Radial distribution of H_2O mass fraction at x = 100mm.

The work is now under progress to use two different chemical models for combustion (the flamelet model and the chemical equilibrium model) and train two different neural networks (with using larger training sample domain for increasing the accuracy of neural predictions) and compare the results for each chemical assumption.

REFERENCES

1. BARITAUD, T., POINSOT, T. and BAUM, M. *Direct Numerical Simulation for Turbulent Reacting Flows*, 1996, Editions Technip, Paris.
2. RHODES, R.P. A probability distribution function for turbulent flows, *Turbulent Mixing in Non-Reactive and Reactive Flows*, MARTHY, S.N.B. (Ed), Plenum Press, 1975.
3. POPE, S.B. Computationally efficient implementation of combustion chemistry using in situ adaptive tabulation, 1996, Sibley School of Mechanical and Aerospace Engineering Report, FDA 96-02.
4. MAAS, U. and POPE, S. Simplifying chemical kinetics: intrinsic low-dimensional manifolds in composition space, *Combustion and Flame*, 1992, **88**, pp 239-264.
5. SHIH, T.H., LIOU, W.W., SHABBIR, A., YANG, Z. and ZHU, *J Comput. Fluids*, 1995, **24**, (3), pp 227-238.
6. YAGA, M., and SASADA, K. An eddy characteristic time modeling in LES for gas turbine combustor, July 2000, Proceedings International Joint Power Generation Conference, Miami Beach, Florida, pp 23-26.
7. MERCI, B., DE LANGHE, C., LODEFIER, K. and DICK, E. *J Thermophys Heat Transfer*, 2004, **18**, (1), pp 100-107.
8. CHEN, J.Y., KOLLMANN, W. and DIBBLE, R.W. PDF Modeling of turbulent non-premixed methane jet flames, *Combustion Science and Technology*, 1989, **64**, pp 315-346.
9. MERCI, B. and DICK, E. *Flow Turb Combust*, 2002, **68**, (4), pp 335-358.
10. MERCI, B., NAUD, B. and ROEKAERTS D. Flow and mixing fields for transported scalar PDF simulations of a piloted jet diffusion flame, *Flow Turb Combust*, 2005, **74**, pp 239-272.
11. KARAYIANNIS, N.B. and VENETSANOPOULES, A.N. *Artificial Neural Networks*, 1993, Kluwer Academic Publishers.
12. CHRISTO, F.C., MASRI, A.R. and NEBOT, E.M. Artificial neural network implementation of chemistry simulation of H_2/CO_2 flames, *Combustion and Flame*, 1996, **106**, pp 406-427.
13. LIMIN, F. *Neural Network in Computer Intelligence*, 1994, McGraw-Hill, International Editions.
14. BLASCO J.A., FUEYO, N., DOPAZO, C. and BALLESTER, J. Modeling the temporal evolution of a reduced combustion chemical system with an artificial neural network, *Combustion and Flame*, 1998, **113**, (1/2), pp 38-52 .
15. MERCI, B., DICK, E. and DE LANGHE, C. *Combustion and Flame*, 2002, **131**, (4), pp 465-468.
16. Second Workshop on Aerodynamics of Steady-State Combustion Chambers and Furnaces (ASCF), 28-29 November 1996, Pisa. Final Report. MARIOTTI, G. and TIRIBUZI, S. (Edited), ENEL, Direzione Studi E Richerche, Centro Ricerca Termica.

APPENDIX 1

A non-linear, first order expression for the turbulent stresses in terms of local mean strain rate and vorticity tensors is good to obtain accurate results for a wide variety of flow types:

$$-\bar{\rho}\overline{u_i''u_j''} = 2\mu_t S_{ij} - \frac{2}{3}\rho k\delta_{ij} \quad \ldots (A1)$$

The eddy viscosity is:

$$\mu_t = \rho[c_\mu f_\mu + \frac{c_1}{4}\tau_t^2(\Omega^2 - S^2)]k\tau_t \quad \ldots (A2)$$

Where f_u is a damping function which forces the eddy viscosity to zero at solid boundaries. The turbulent time scale (low-Reynolds formulation):

https://doi.org/10.1017/S0001924000003195 Published online by Cambridge University Press

$$\tau_t = \frac{k}{\varepsilon} + \left(\frac{\mu}{\rho\varepsilon}\right)^{1/2} \quad \ldots (A3)$$

The non-linearity in Equation (A1) can be seen in the second term of Equation (A2), which accounts for the effect of rotation or curvature of streamline.This is captured by:

$$\begin{cases} S \geq \Omega: & c_1 = -\min\{40{c_\mu}^4, 15\} \\ S < \Omega: & c_1 = -\min\{\min\{40{c_\mu}^4, 15\}, \dfrac{4 f_\mu c_\mu}{(\Omega^2 - S^2){\tau_t}^2}\} \end{cases} \quad \ldots (A4)$$

The non-linearity in Equation (A1) is also hidden in the expression for the c_μ, which is Ref 15:

$$c_\mu = \frac{1}{(4 + A_s \eta)} \quad \ldots (A5)$$

with:

$$\begin{aligned} S_{ij} &= \frac{1}{2}\left(\frac{\partial u_i}{\partial x_j} + \frac{\partial u_j}{\partial x_i}\right) - \frac{1}{3} \\ \Omega_{ij} &= \frac{1}{2}\left(\frac{\partial u_i}{\partial x_j} - \frac{\partial u_j}{\partial x_i}\right) \\ S &= \sqrt{2 S_{ij} S_{ij}} \\ \Omega &= \sqrt{2 \Omega_{ij} \Omega_{ij}} \\ A_s &= \sqrt{3}\,\mathrm{Cos}\varphi \\ \varphi &= \frac{1}{3}\mathrm{Cos}^{-1}(\sqrt{6} W) \end{aligned} \quad \ldots (A6)$$

Looking at the transport equations for k and ε, Equation (2) shows that the transport equation for k is standard and the model parameters are given in Table (2). All of them are standard or retrieved from Ref. 15, with the exception of $c_{\varepsilon 2}$. This parameter contains a rotation term and makes sure that the ε transport equation remains consistent for high rotation terms. In ε transport equation, f_{R_y} is called the blending function and it is based on the normalised distance $R_y = \rho y \sqrt{k} / \mu$ from the nearest solid boundary.

The low Reynolds source term E, is described in Ref. 16:

$$E = -1 \cdot 8(1 - f_\mu)\left(\mu + \frac{\mu_t}{\sigma_\varepsilon}\right)\frac{\partial k}{\partial x_p}\frac{\partial \tau_t^{-1}}{\partial x_p} \quad \ldots (A7)$$

This term is non-zero near the nozzle exit due to the factor $1 - f_\mu$.

APPENDIX 2

The power of the mixture fraction modelling approach is that, the chemistry is reduced to one conserved mixture fraction. All thermo-chemical scalars (species mass fraction, density, and temperature) are, uniquely, related to the mixture fraction. The instantaneous mixture fraction value at each point in the flow field can be used to compute the instantaneous values of individual species mole fractions, density, and temperature. As shown below, these instantaneous values of mass fractions, density, and temperature depend, solely, on the instantaneous mixture fraction:

$$\phi_i = \phi_i(f) \quad \ldots (A8)$$

where ϕ can be mass fractions, density or temperature.

The probability density function, $p(f)$, describes the temporal fluctuations of f in the turbulent flow and it is used to compute time-averaged values of variables, that depend on f.

$$\bar{\phi}_i = \int_0^1 p(f)\phi_i(f)\mathrm{d}f \quad \ldots (A9)$$

For the shape of PDF, we used the β-function. The shape produced by this function depends, solely, on the mean mixture fraction and its variance.

$$p(f) = \frac{f^{\alpha-1}(1-f)^{\beta-1}}{\int f^{\alpha-1}(1-f)^{\beta-1}\mathrm{d}f} \quad \ldots (A10)$$

where:

$$\alpha = \bar{f}\left(\frac{\bar{f}(1-\bar{f})}{\bar{f}'^2} - 1\right) \quad \ldots (A11)$$

$$\beta = (1-\bar{f})\left(\frac{\bar{f}(1-\bar{f})}{\bar{f}'^2} - 1\right)$$

https://doi.org/10.1017/S0001924000003195 Published online by Cambridge University Press